Materials & Design 231 (2023) 112027

Contents lists available at ScienceDirect

Materials & Design

journal homepage: www.elsevier.com/locate/matdes

Exploring the design space of the effective thermal conductivity, permeability, and stiffness of high-porosity foams

Silven Stallard [a], Huan Jiang [b], Yanyu Chen [b], Theodore L. Bergman [a], Xianglin Li [a,c,*]

[a] Department of Mechanical Engineering, University of Kansas, Lawrence, KS 66045, USA
[b] Department of Mechanical Engineering, University of Louisville, Louisville, KY 40292, USA
[c] Department of Mechanical Engineering and Materials Science, Washington University in St. Louis, St. Louis, MO 63130, USA

HIGHLIGHTS

- We developed graphical thermal conductivity, permeability, and stiffness comparisons to clearly illustrate structurally dependent properties.
- These property charts can aid additive manufacturing in selecting porous structures for diverse applications.
- This study compares stochastic foams, lattice-based BCC, shell-based TPMS, and hybrid foam composed of beam and shell with adjustable parameters.
- Different high-porosity and open-cell foam structures can be grouped on the charts based on their unique properties.

GRAPHICAL ABSTRACT

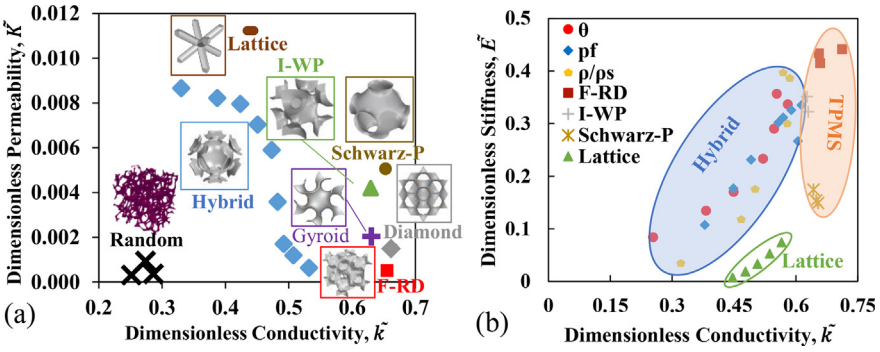

ARTICLE INFO

Article history:
Received 22 February 2023
Revised 18 April 2023
Accepted 20 May 2023
Available online 22 May 2023

Keywords:
Architected foams
Thermal conductivity
Permeability
Stiffness
TPMS
BCC lattice
Porous media

ABSTRACT

With knowledge of only a few effective properties of a porous structure, the applicability of the structure for a given system can quickly be determined. This study numerically simulates the effective thermal conductivity, permeability, and stiffness of high porosity structures. Commonly used isotropic architected porous structures are compared with commercially available stochastic metal foams. The architected structures include body-centered cubic (BCC) lattice, shell-based triply periodic minimal surface (TPMS), and hybrid foam (HF) composed of beam and shell with multiple adjustable parameters. The simulated effective properties touch on the applicability in heat transfer, fluid flow, and mechanically stressful situations. The dimensionless effective properties of the structures are presented in graphical form to clearly illustrate structurally dependent properties. Compared to the stochastic metal foams, the architected structures (BCC, TPMS, and most HF) showed higher effective thermal conductivities and permeabilities. This indicates a potential to improve the efficiency of a thermal or fluid flow system by replacing the stochastic foam with architected foam. Additionally, the HF structure shows broad tunability of specific properties. All effective properties simulated were rendered dimensionless to only reflect the impact of topology, and plotted in charts to show trends. These charts can aid in the selection of porous structures in diverse applications.

1. Introduction

The study and use of porous structures are spread widely throughout many industries and can be found in scientific fields

* Corresponding author at: Department of Mechanical Engineering, University of Kansas, Lawrence, KS 66045, USA.
E-mail address: lxianglin@wustl.edu (X. Li).

https://doi.org/10.1016/j.matdes.2023.112027
0264-1275/

Nomenclature

b	leading coefficient
c	specific heat
C_1	1st order coefficient
C_2	2nd order coefficient
C_ε	porosity dependent coefficient
d	diameter
D_p	base size of the unit cell
E	Young's modulus
$\boldsymbol{F}$	deformation gradient tensor
$\boldsymbol{H}$	macroscopic displacement gradient tensor
$\underset{\sim}{k}$	thermal conductivity
k	dimensionless thermal conductivity
$\underset{\sim}{K}$	permeability
K	dimensionless permeability
p	pressure
pf	perforation factor
q''	heat flux
$\boldsymbol{s}$	displacement
S	dimensionless slope of thermal conductivity
T	temperature
t	time
$\boldsymbol{u}$	velocity
$\boldsymbol{x}$	position

Subscripts

Al	aluminum
eff	effective
f	fluid
para	parallel configuration of materials
s	solid
ser	series configuration of materials

Greek

α	exponential coefficient
β	inertia coefficient
ε	strain
θ	binder angle
μ	dynamic viscosity
ν	Poisson's ratio
ρ	density
ψ	sphericity
φ	porosity

that range from geology [1–4] to biomedical engineering [5–9]. These porous structures utilize their high porosity and light weight to provide effective properties that are advantageous for a given application, such as, but not limited to thermal insulation, thermal dissipation, cushioning, and energy absorption. These effective properties vary, depending on the type of porous structure, so the selection of the porous structure type is paramount for maximizing the effectiveness of a system.

Conventionally, stochastic metal foams have been intensively used and studied due to a strong demand for lightweight materials [10]. Extensive studies of stochastic metal foams have investigated their suitability for thermal and mechanical applications. In one study, the heat dissipation capability of stochastic metal foams was investigated experimentally and numerically; it was shown that heat transfer in copper foams is more sensitive to cell size than relative density [11]. Moreover, the same study developed a numerical model for forced convection across open-celled metal foams to predict how changing different parameters would change the heat transfer [11]. In another study to analyze the effect of geometric parameters, researchers derived an empirical formula for the effective thermal conductivity of stochastic aluminum foam from systematic numerical simulations with different pore sizes and porosities [12]. Although this study analyzed the effect of geometric parameters, the limited ability to control those parameters in stochastic foams has largely hindered their further development.

In contrast to stochastic foams, architected materials (AM) have the advantage of highly regular and controllable geometries. The geometric features of such structures can be tailored for a specific application or optimized for permeability, effective thermal conductivity, stiffness, and mechanical strength [13]. These advantages, along with advances in additive manufacturing techniques, point toward AM structures replacing the stochastic in future implementations.

Many architected material structures exist, including the lattice-based simple-cubic (SC), body-centered-cubic (BCC), and face-centered-cubic (FCC) cellular structures. The lattice-based structures provide better interconnected and regular structures that are directly controllable in their manufacture. Another set of porous media structures currently being explored [14–21] is the triply periodic minimal surface (TPMS) structure. A TPMS is a naturally occurring surface shape that is periodic in three dimensions with zero mean curvature and minimal surface area between any set of given boundaries [14,15]. These surfaces can be completely defined by mathematical equations and can be offset to describe structures of a given characteristic solid phase thickness. Recent advances in additive manufacturing have allowed these complex structures to be fabricated and studied to explore their potentially advantageous properties [16].

Wang et al. [17] compared the effective thermal and mechanical properties of stochastic commercial aluminum foams with those of a TPMS structure, and found that the TPMS structure had 103% higher thermal conductivity as well as 488% higher stiffness [17]. Qureshi et al. [18] incorporated phase change material (PCM) within TPMS structures and conventional metal-foam-based thermal management systems. The study focused on the benefits in conduction-only cases and cases with both natural convection and conduction. In both thermal situations, the TPMS structures performed better than the conventional metal foam [18,19]. Vignoles and coauthors simulated several TPMS structures, considering conduction and radiative heat transfer effects using a hybrid random walk numerical method [20,22]. Vignoles showed that for applications of TPMS in which radiative heat transfer can occur, overall heat transfer can be significantly affected due to the large surface area of the TPMS.

The hybrid foam (HF) structure, designed by Jiang et al. [23], was selected for this study due to its geometric flexibility, allowing for property optimization. A previous study of the effective mechanical properties of HF proved that the structure can exhibit an increase in its stiffness by an order of magnitude, while increasing its relative density by only 5% [23]. Whereas the other architected structures examined in this study have only two parameters to vary (scale and porosity via thickness), the HF design has two additional parameters that can increase the range of properties achievable.

This study reports pore-scale simulations of the strut-based BCC lattice, HF, and sheet-based TPMS structures to reveal accurate

effective thermal conductivity, permeability, and mechanical stiffness trends among different structure types. The properties are rendered dimensionless to define the intrinsic geometric properties of the structures, regardless of material type, porosity, or size.

2. Models

2.1. Geometric models

Three types of porous structures were defined via a 3D CAD tool and tested in this study: lattice-based structures with BCC symmetry, shell-based TPMS structure, and HF composed of beam and shell. As will become evident, the BCC lattice structures were created using simple cylindrical rods in the BCC unit cell structure layout. The only alterable aspect of this structure is the rod diameter, which was adjusted to achieve the desired relative density. The TPMS structures are based on surfaces defined by mathematical equations. The surfaces defined are then offset by a certain distance to provide room for a solid phase to reside between the surfaces. The thickness offset is the only adjustable parameter of each of the TPMS structures, which directly controls the given structure's porosity. The TPMS structures were created using the Grasshopper plugin in Rhino3D (version 7) [24] and the software nTopology (version 3.31) [25]. The structures in this study include Schwarz-P, F-RD, I-WP, Gyroid, and Diamond [16].

The HF structure, created by Jiang et al. [23] is described in their 2020 paper, and the majority of its description is omitted here for brevity. The structure allows for significant parameter adjustment, increasing the potential to optimize the design for a given application. The parameters investigated here, listed in Table 1, are intended to match the parameters used in the original mechanical property investigation on a unit cell with the lattice size of 25 mm [23] as well as to add additional points for trend exploration. When varying the TPMS and lattice structures, the only parameter that was varied was the thickness of the solid phase, leading to different porosities. Detailed equations and descriptions of how the HF design was created can be found in the original publication [23]. The relative density parameter is controlled by altering the thickness, *th*, and the perforation factor is controlled by altering the radius of the perforating hole, *r*, where $pf = r/R$. Diagrams to aid in comprehension of these parameters are provided in Fig. 1.

Table 1
Parameter values used to create HF structure sets.

	Thickness, *th* [mm]	Binder Angle, θ [degrees]	Perforation Factor, *pf* [/]
$\theta = 5$	1.039	5	0.4
$\theta = 7.5$	1.039	7.5	0.4
$\theta = 10$	1.039	10	0.4
$\theta = 15$	1.039	15	0.4
$\theta = 20$	1.039	20	0.4
$\theta = 30$	1.039	30	0.4
$\theta = 40$	1.039	40	0.4
$\rho/\rho_s = 0.03$	0.100	20	0.4
$\rho/\rho_s = 0.05$	0.250	20	0.4
$\rho/\rho_s = 0.08$	0.500	20	0.4
$\rho/\rho_s = 0.13$	1.053	20	0.4
$\rho/\rho_s = 0.20$	1.878	20	0.4
$\rho/\rho_s = 0.31$	4.988	20	0.4
$pf = 0.20$	1.039	20	0.2
$pf = 0.30$	1.039	20	0.3
$pf = 0.35$	1.039	20	0.35
$pf = 0.375$	1.039	20	0.375
$pf = 0.40$	1.039	20	0.4
$pf = 0.45$	1.039	20	0.45
$pf = 0.50$	1.039	20	0.5
$pf = 0.55$	1.039	20	0.55
$pf = 0.60$	1.039	20	0.6

The last structure in this study, stochastic metal foam, provides a common frame of reference. Effective property values for stochastic metal foam samples were calculated in previous studies [26,27]. The results of the former studies are applied in this paper. A sample unit cell of each type of geometric model is shown in Fig. 2, as well as a representative volume of a commercially available stochastic metal foam.

2.2. Models of effective properties

When considering the effective properties of porous materials, it is often convenient to utilize bulk volume-averaged descriptions that assume the same effective property throughout isotropic porous materials. Such models are simple to apply and computationally inexpensive to use. The effective properties of a porous structure could be obtained by several methods, such as empirical correlations, analytical solutions, pore-scale simulations, and statistical models. Empirical correlations relate the effective properties to the simplified pore-scale geometry of the structure. For example, the Kozeny-Carman equation can be used to predict permeability, assuming laminar flow [1], while the Brooks-Corey equation can be used for capillary pressure[2]. Many analytical and empirical equations have been derived to calculate the effective thermal conductivity [26,28,29]. All these empirical correlations are based on important assumptions that, when not met, can cause the resulting effective property values to be significantly in error.

Numerical approaches such as computational fluid dynamics (CFD) and finite element analysis (FEA) can also be used to predict local quantities within the structure at discrete locations, such as temperature or pressure, ideally resulting in a more accurate understanding of overall behavior. Such approaches can also be used to calculate the effective properties of the physical structure. Using a random walk theory, a universal predictive model for the effective thermal conductivity of porous media was created with only an image of the pore-scale geometry and the thermal conductivity of the phases as inputs [26]. Random walk models are relatively computationally inexpensive but can generate predictions of low accuracy. Meanwhile, pore-scale heat transfer simulations have been reported to require days of computation time to generate predictions of one case [19]. As with all simulations, a balance between fidelity and cost is required for most situations.

2.2.1. Thermal conductivity

To determine the effective thermal conductivity of a given porous structure, a single unit cell was imported to Star CCM+ (version 2020.3), and run through a steady-state, conduction-based heat transfer simulation. Considering only conduction in the solid phase, the heat equation is:

$$\nabla \cdot (k_s \nabla T) = 0 \tag{1}$$

where k_s is the thermal conductivity of the solid. This simulation assumes that the interstitial regions have a thermal conductivity of zero.

All unit cells considered in this study are symmetric about the *x*-, *y*-, and *z*-axes, with the origin of the coordinate system located at the center of the unit cell. The boundary conditions were specified to allow for the simple calculation of the effective thermal conductivity, k_{eff}, using:

$$k_{eff} = \frac{q''}{(T_H - T_L)/\Delta x} \tag{2}$$

where *q*" is the average heat flux along the *x*-axis, Δx is the distance across the system in the *x*-direction, and T_H and T_L are the temper-

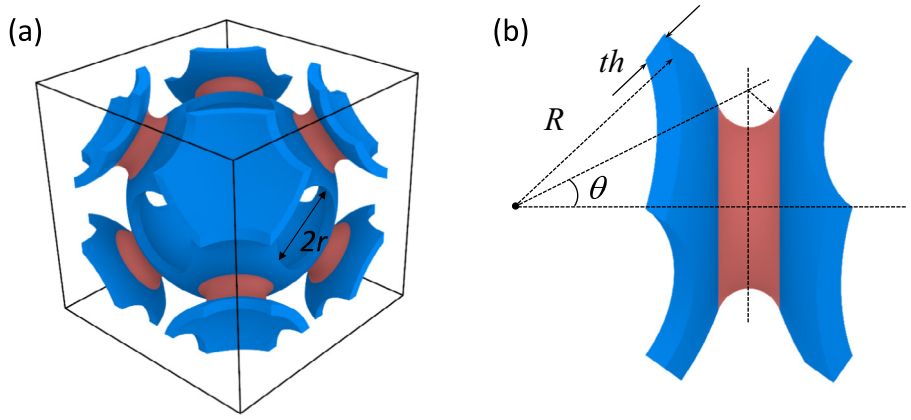

Fig. 1. In a), the HF unit cell is shown where r is the perforating hole radius. In b), the binder angle, θ, is shown along with the thickness, th.

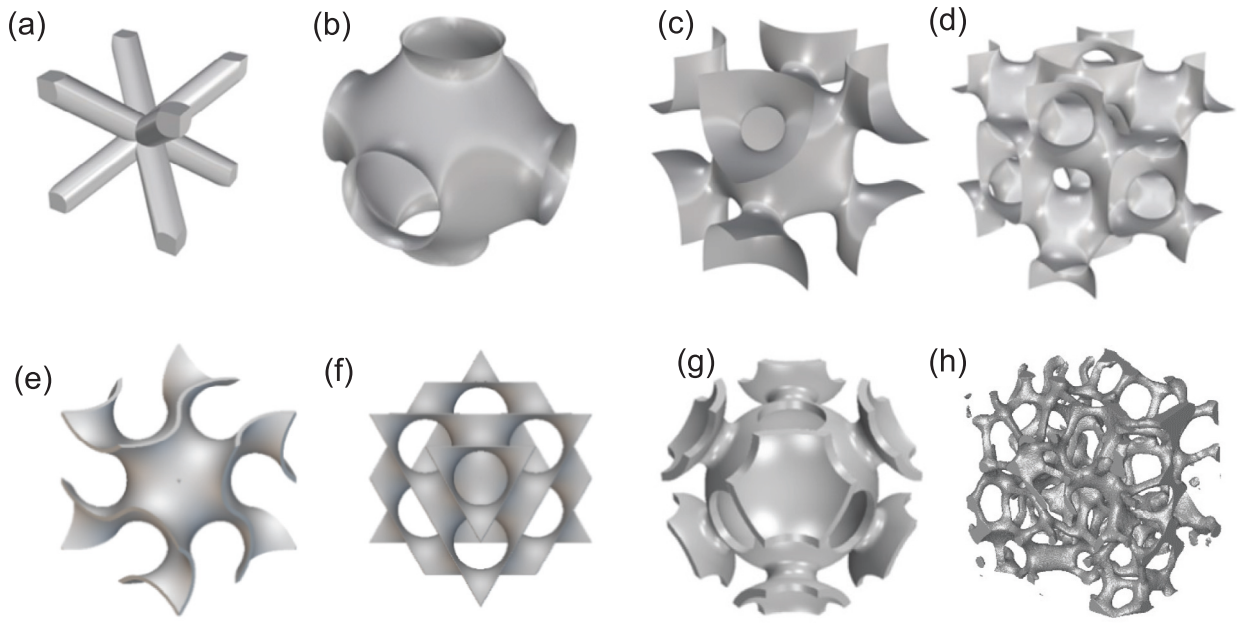

Fig. 2. A repeatable, isotropic unit cell of (a) lattice-based structure with BCC symmetry, followed by the TPMS-based structures such as (b) Schwarz-P, (c) F-RD, (d) I-WP, (e) Gyroid, and (f) Diamond, (g) the HF structure, and the (h) stochastic metal foam structure [24,25].

atures at the left and right boundaries, respectively. All remaining boundaries are adiabatic, as shown in Fig. 3.

A mesh independence study was conducted by adjusting the element count of the mesh between 44,715 to 3,104,476 elements. There was less than 0.1% difference between the average heat flux for a mesh of 296,508 elements and that of a mesh with 572,623 elements. Therefore, the predictions for the mesh consisting of 296,508 elements are considered independent of the mesh size. The exact element count varied between designs, but the mesh size was always on the order of 300,000. Validation testing was performed by comparing the analytical solution for the two-phase parallel configuration [30] with the numerical solutions of the model of this study.

2.2.2. Permeability

To determine the permeability of a given structure, six unit cells were aligned in the flow direction, as shown in Fig. 4. The steady-state, isothermal, fluid flow simulation was performed using Star CCM +. The simulation includes the following governing equations for continuity:

$$\nabla \cdot \left(\rho \vec{\boldsymbol{u}}\right) = 0 \tag{3}$$

and linear momentum:

$$\rho\left(\vec{\boldsymbol{u}} \cdot \nabla\right) \vec{\boldsymbol{u}} = -\nabla p + \mu \nabla^2 \vec{\boldsymbol{u}} \tag{4}$$

where ρ is the density, $\vec{\boldsymbol{u}}$ is the local velocity, p is the pressure, and μ is the dynamic viscosity of the fluid. The model geometry is defined by the liquid phase that fills the porous structures.

Symmetry boundary conditions are applied to all boundaries of the computational domain except at $x = 0$ and $x = L$, as shown in Fig. 4. Uniform and equal velocity distributions were specified at the inlet and outlet to create a fluid flow through the structure. With the pressure difference between the inlet and outlet determined at multiple inlet velocities, a second-order polynomial trendline can be fitted to the data points. The permeability can

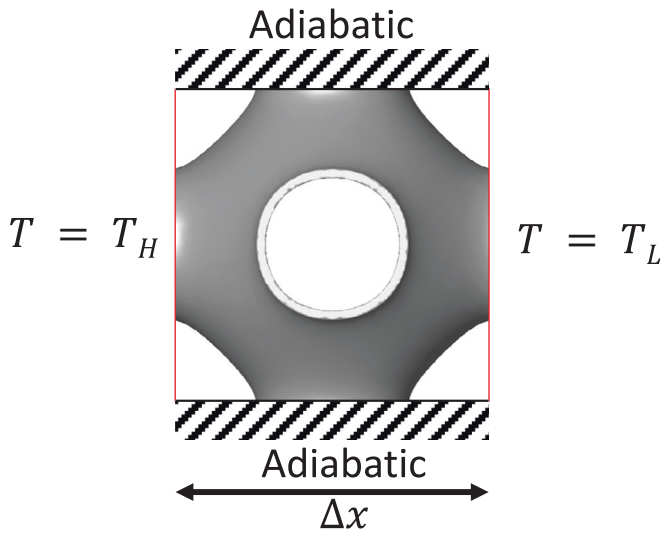

Fig. 3. Diagram of the effective thermal conductivity simulation boundary conditions with a Schwarz-P unit cell.

then be calculated by matching the first-order coefficients of the Darcy-Forchheimer's equation with the trendline:

$$\frac{p_i - p_o}{\Delta x} = -\frac{dp}{dx} = \frac{\mu}{K}\left(\varphi\vec{\boldsymbol{u}}\right) + \beta\frac{\rho}{\sqrt{K}}\left(\varphi\vec{\boldsymbol{u}}\right)^2 = C_1\left(\varphi\vec{\boldsymbol{u}}\right) + C_2\left(\varphi\vec{\boldsymbol{u}}\right)^2 \quad (5)$$

where K is the permeability, β is the inertia coefficient, φ is the porosity of the structure, $\vec{\boldsymbol{u}}$ is the velocity of the inlet flow, and p_i and p_o are the pressure at the inlet and outlet, respectively. This results in a calculation of permeability via the equation:

$$K = \frac{\mu}{C_1} \quad (6)$$

where C_1 is the first-order coefficient from Equation (5). Using the calculated permeability, it is possible to solve for the inertia coefficient, β, via the equation:

$$\beta = \frac{C_2\sqrt{K}}{\rho} \quad (7)$$

The simulations were tested for grid independence, with element counts varying from 720,000 to 14,000,000. The number of unit cells needed for convergence of the permeability value was also varied from 1 to 12. As a result of this convergence testing, six unit cells were used in all permeability simulations, consistent with Fig. 4. As with the mesh used for the effective thermal conductivity simulations, the permeability simulation mesh varied between designs, but was always on the order of five million elements. For all cases, the solid phase was specified to be aluminum, and the interstitial matter (in the permeability testing only) was specified to be liquid water, with the properties for each listed in Table 2.

2.2.3. Stiffness

FEA simulations were conducted to obtain the effective stiffness for different architectures. The stiffness is defined by the slope of the initial linear part of a stress–strain curve:

$$E = \sigma/\varepsilon \quad (8)$$

when the stress, σ, and strain, ε, are in the elastic range. In the simulations, aluminum was used as the solid with $E = 70GPa$ and $v = 0.33$. All of the structures simulated were meshed with $\sim$ 100,000 tetrahedral elements (C3D4) using Hypermesh (Altair Engineering Inc, USA). In order to eliminate the effect of boundary conditions on the simulated results for the different lattice architectures, mechanical periodic boundary conditions (PBC) were applied to the representative volume element (RVE), as shown in Fig. 5. To subject an RVE to a macroscopic deformation gradient, PBC can be described by the following equation:

$$\boldsymbol{s}(B) - \boldsymbol{s}(A) = (\boldsymbol{F} - \boldsymbol{I})[x(B) - x(A)] = \boldsymbol{H}[x(B) - x(A)] \quad (9)$$

where A and B are two points periodically located on the RVE boundary, $\boldsymbol{s}$ denotes the displacement, x represents the position in the reference configuration, $\boldsymbol{F}$ is the deformation gradient tensor, and $\boldsymbol{H} = \boldsymbol{F} - \boldsymbol{I}$ is the macroscopic displacement gradient tensor. Here, $\boldsymbol{H}$ can be expressed by the following equation:

$$\boldsymbol{H} = \begin{bmatrix} H_{11} & H_{12} & H_{13} \\ H_{21} & H_{22} & H_{23} \\ H_{31} & H_{32} & H_{33} \end{bmatrix} = \begin{bmatrix} F_{11} - 1 & F_{12} & F_{13} \\ F_{21} & F_{22} - 1 & F_{23} \\ F_{31} & F_{32} & F_{33} - 1 \end{bmatrix} \quad (10)$$

The macroscopic deformation is imposed by specifying nine components of $\boldsymbol{H}$, which are perceived as generalized degrees of freedom operationally applied using the virtual nodes. The macroscopic first Piola-Kirchoff stress tensor and the corresponding macroscopic Cauchy stress tensor are extracted through the virtual work principle [31–33]. The relative stiffness can be obtained by homogenization methods. This model was validated using honeycomb structures [34] whose mechanical stiffness can be analytically defined.

3. Results and discussion

The HF design has shown great potential as a lightweight porous structure with desirable effective mechanical properties [23]. In thermal management situations, weight and strength are often significant factors in how valued a porous structure is, but the material's effective thermal properties are usually of the most significance. During the investigation of a structure's effective thermal properties, alternative porous media structures were evaluated to establish a more holistic perspective on the HF design's value.

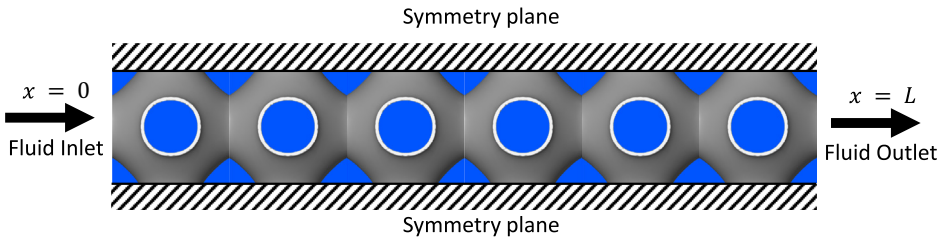

Fig. 4. Diagram of the permeability simulation boundary conditions with Schwarz-P unit cells. Grey is solid and blue is liquid. (For interpretation of the references to colour in this figure legend, the reader is referred to the web version of this article.)

Table 2
Values of material properties used in the simulations. All material properties were assumed to be constant.

Material Property of Aluminum	**Value**	**Units**
Thermal Conductivity	237	W m^{-1} K^{-1}
Specific Heat	903	J $kg^{-1}K^{-1}$
Density	2702	kg m^{-3}
Material Property of Water	**Value**	**Units**
Thermal Conductivity	0.62	W m^{-1} K^{-1}
Specific Heat	4180	J $kg^{-1}K^{-1}$
Density	998	kg m^{-3}
Dynamic Viscosity	8.89E-4	Pa s

shown in Fig. 6. The k_s term was set to the thermal conductivity of aluminum, given in Table 2. The thermal conductivity of the fluid, k_f, is zero in these simulations.

The effective thermal conductivities associated with the HF parameters of Table 1, such as binder angle, relative density, and perforation factor, are reported in Fig. 6a. A clear linear trend emerges for HF structures with binder angles between 15 and 40 degrees, relative densities between 0.03 and 0.31, and perforation factors between 0.2 and 0.6. This linear trend is represented among the other structure types in Fig. 6b by the S = 0.48 dotted line.

As shown with the HF structures in Fig. 6a, the linear trendline

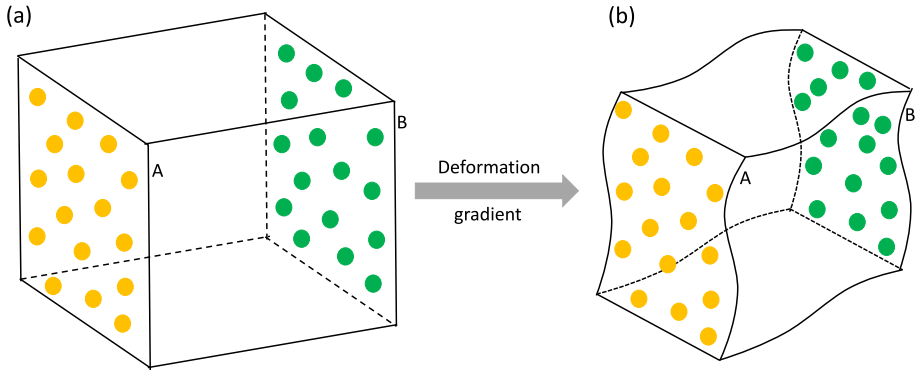

Fig. 5. Schematics of applying periodic boundary conditions.

3.1. Effective thermal conductivity results

The effective thermal conductivity of a porous medium composed of solid and liquid phases has theoretical lower and upper limits as expressed by:

$$k_{\text{eff,ser}} = \frac{1}{\frac{\varphi}{k_f} + (1-\varphi)/k_s} \tag{11}$$

and:

$$k_{\text{eff,para}} = \varphi \cdot k_f + (1-\varphi) \cdot k_s \tag{12}$$

respectively, where φ is the porosity, k_f is the thermal conductivity of the fluid, and k_s is the thermal conductivity of the solid [30]. Using Equations (11) and (12) to define limiting behavior, the effective thermal conductivity results of all porous media simulated are can be fitted to the effective thermal conductivity. In the same fashion, fitting linear regression lines for each of the structure types (while setting the intercept to zero to match the physics of the system), the data can be described by two parameters: the slope of the trendline and the R^2 value. These two parameters, for each of the structure types, can be found in Table 3, where the dimensionless slope, S, is described by the equation:

$$S = \frac{1}{k_s}\frac{d(k_{\text{eff}})}{d(\rho/\rho_s)} \tag{13}$$

where k_s is the thermal conductivity of the material composing the solid phase.

The dimensionless slope represents the intrinsic ability of the structure to transmit heat via conduction. The stochastic metal foam structures correspond to commercially available structure

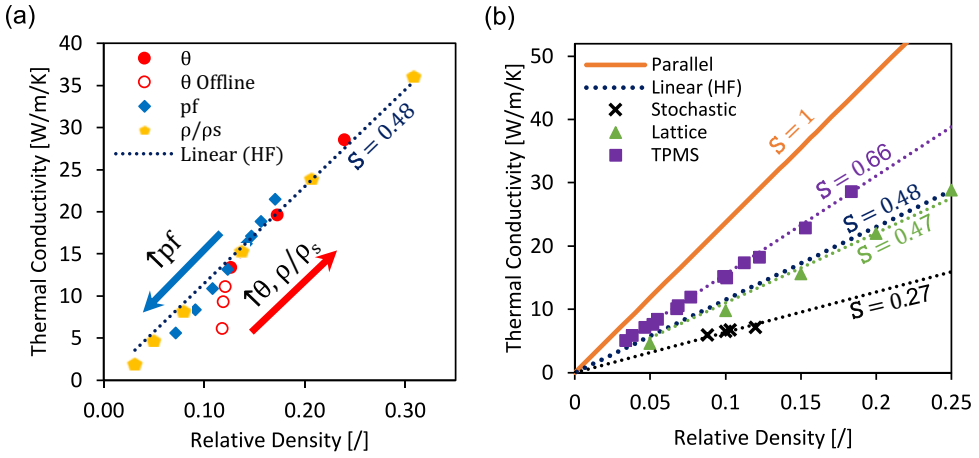

Fig. 6. The effective thermal conductivity versus relative density for a) the hybrid foam parameter datasets and a trendline of all but the offline data ($\theta = 5, 7.5, 10$), and the b) all studied structures and their linear regression trendlines, with the hybrid foam structures represented solely by the trendline from a).

Table 3
Dimensionless slopes and R^2 values associated with Fig. 6b.

	TPMS	HF	Lattice	Stochastic	Units
S	0.6555	0.4829	0.4651	0.2692	[/]
R^2	0.9994	0.9981	0.997	0.9976	[/]

options (40-, 20-, 10-, 5-PPI) and have the lowest conductivity at a given relative density. Even though the stochastic structures are represented by only four data points, the results are sufficient to show the unstructured metal foams' effective thermal conductivities fall well short of the effective thermal conductivities of better connected, regular structures of a repeating pattern. Specifically, the lattice and the HF effective thermal conductivities reach approximately 50% of the theoretical maximum values. The TPMS structures exhibit the highest dimensionless slope, ~0.66, closely matching the 0.61 value from Vignoles et al. [20], the 2/3 coefficient from Schuetz and Glicksman [35], and most of the curve-fitting TPMS values from Abueidda et al. [21]. Although the TPMS dataset included five different types of structures (F-RD, I-WP, Schwarz-P, Gyroid, and Diamond), it provides an R^2 fitted trendline value of 0.9994. The mathematical conditions that define a TPMS, minimal surface area between any set of given boundaries and zero mean curvature, describe a structure with consistently high effective thermal conductivity in three dimensions, regardless of the specifics of the equation or TPMS type.

3.2. Permeability results

Altering the relative density over a narrow range at the small values considered here should not significantly affect the permeability of the structure, so only one structure of each type of TPMS, one lattice structure, along with the HF dataset with different perforation factors, are compared. The permeabilities of three stochastic metal foam structures were compared using the values from Wang et al. [17]. The perforation factor parameter alters the size of the perforating hole in the HF structure, so it is likely to have the most significant effect of all the parameters on permeability.

Permeability is a function of pore size, making it difficult to directly compare the permeability values of porous media of various scales. However, the Kozeny-Carman equation can, as a first approximation, be used to analyze the media considered here:

$$K = \psi^2 \frac{\varphi^3 D_p^2}{150(1-\varphi)^2} \tag{14}$$

where φ is the porosity and ψ is the sphericity of the particles in a packed bed. This equation can be simplified to:

$$K = C_\varphi D_p^2 \tag{15}$$

where C_φ is a porosity dependent coefficient. Therefore, the permeability should scale approximately with D_p^2 where D_p is the base unit cell size. The base unit cell size of the HF structure was varied from 2.5 mm to 35 mm, the permeability associated with each size was simulated and calculated, and the results are shown in Fig. 7.

The resulting trendline evident in Fig. 7 shows that the HF structure follows the expected behavior of K consistently varying with the base unit cell size, D_p. This makes it possible to compare the permeability of the HF structure to permeabilities of porous media of a different scale.

The permeability and effective thermal conductivity of the structures simulated are reported in Fig. 8. Plotting the permeability of each structure against its effective thermal conductivity might result in an intuitive thermal property plot. However, if certain characteristics are not taken into account, such as porosity and

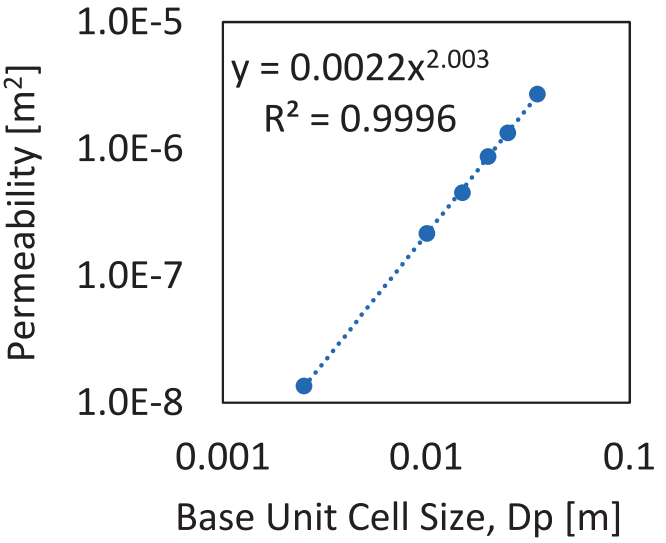

Fig. 7. The predicted permeability of the HF structures with various unit cell sizes.

scale of the medium, a potentially misleading graph, as shown in Fig. 8a may result. The stochastic foams have smaller pore sizes, therefore, lower permeability than the other structures in Fig. 8a. Some of the TPMS structures have lower thermal conductivity than the HF structures due to a higher porosity. This could lead to the conclusion that those TPMS structures have lower conductivity than HF structures, which is in contrast to the results shown in Fig. 6b.

To properly compare the permeabilities of the porous media, the pore size must be accounted for using the relationship shown in Fig. 7. The solid material thermal conductivity and porosity must be considered for effective thermal conductivity values. Both the permeability and effective thermal conductivity have been rendered dimensionless using the equations:

$$\tilde{K} = \frac{K}{{D_p}^2} \tag{16}$$

and:

$$\tilde{k} = \frac{k_{eff}}{k_s(1-\varphi)} \tag{17}$$

where the $\tilde{K}$ is the dimensionless permeability and the $\tilde{k}$ is the dimensionless effective thermal conductivity. The non-dimensional conductivity and permeability are shown in Fig. 8b. The TPMS structures (F-RD, I-WP, Schwarz-P, Gyroid, and Diamond) have higher dimensionless thermal conductivities than the HF structures, and the stochastic foam has a dimensionless permeability comparable to the other structures.

Plotting the permeabilities and effective thermal conductivities in their dimensionless form, as shown in Fig. 8b, separates the porous media performance into four distinct regions: stochastic, HF, lattice, and TPMS structures. The TPMS structures exhibit dimensionless permeabilities and inertia coefficients of 0.00153 to 0.00508 and 0.224 to 0.267, respectively, while the values for the HF perforation factor set range from 0.00053 to 0.00808 and

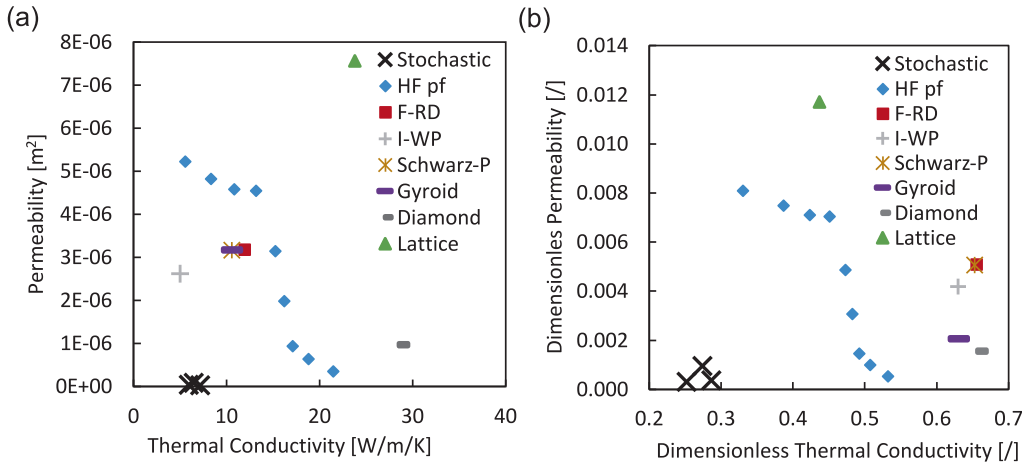

Fig. 8. The a) permeability versus thermal conductivity and the b) dimensionless permeability versus the dimensionless thermal conductivity.

0.162 to 0.400, respectively. All three stochastic foams have dimensionless permeabilities on the order of the lowest TPMS and HF structures: 0.00093, 0.00036, and 0.00031. The lattice structure has the highest dimensionless permeability with a value of 0.01171 and an inertia coefficient of 0.128. Although TPMS structures generally have low permeability, their high thermal conductivities are desirable for specific applications. In comparison, the HF structures have a large range of permeability and a reasonably high dimensionless thermal conductivity. Similar to the HF, the lattice structure has a reasonably high thermal conductivity, and an even higher permeability. It bears noting that the permeability values, high or low, do not necessarily define a corresponding high or low rate of mixing for the structures.

3.3. Mechanical results

In a previous investigation, it was shown that the HF structure outperforms the stochastic foams significantly in terms of both thermal properties and mechanical properties [17]. In this study, the focus is on the comparison of different architected structures. In order to take into consideration the different relative densities of these disparate designs, Fig. 9a shows the normalized relative stiffness (relative stiffness/relative density) as a function of normalized relative thermal conductivity for different HF, lattice, and TPMS structures. The normalized relative stiffness was calculated using the equation:

$$\tilde{E} = \frac{E_{\text{rel}}}{\rho/\rho_s} \tag{18}$$

where E_{rel} is the relative stiffness. The lattice structures show good relative conductivity; however, the relative stiffness is notably lower than that of the HF and TPMS. The HF with different perforations, binder sizes, and relative densities show similar trends of relative stiffness as a function of relative conductivity, which demonstrates a significantly broad range of improvement for relative stiffness and relative conductivity. The TPMS displays good stiffness and conductivity properties; however, it is limited to a low range of tunability compared to HF, as can be observed in the highlighted area in the Ashby plot in Fig. 9a.

Fig. 9b shows the scaling law for different architectures that is described by the relation:

$$\frac{E}{E_s} \propto \left(\frac{\rho}{\rho_s}\right)^n \tag{19}$$

where the subscript, s, represents the physical properties of bulk material. The values of the exponents of the scaling law for different architectures are shown in Table 4. The lattice structure exhibits a power exponent of 2.411, which is consistent with an existing study [36]. This reveals that the lattice is strongly bending-dominated, and it explains why the lattice structure shows inferior relative stiffness. All the other architectures shown in Fig. 9b present exponents ranging from 1.101 to 1.612, which demonstrates stretching-

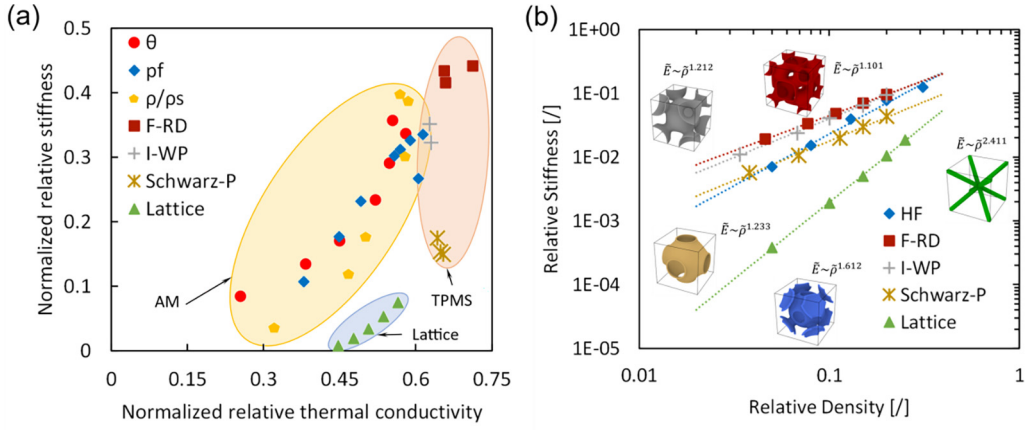

Fig. 9. Mechanical properties of different architectures. (a) Relative stiffness/relative density as a function of relative conductivity/relative density. (b) Scaling law.

Table 4
Power law trendline coefficients and R^2 values from Fig. 9b.

	n
HF	1.612
F-RD	1.101
I-WP	1.212
Schwarz-P	1.233
Lattice	2.411

dominated behavior. This agrees with the preceding discussion of the superior stiffness of HF and TPMS structures. Although the TPMS is featured with excellent stretching-dominated behavior, its inferior low tunability of relative stiffness and conductivity compared to HF neutralize its ideal candidate for multifunctional architectures with desirable stiffness and conductivity.

4. Conclusions

Three types of structures were simulated to determine how their geometric properties are related to their thermal and mechanical behavior. The results of the simulations, when compared to results from the literature for stochastic metal foam, illustrate the advantages that structured porous media could offer. By rendering all properties dimensionless, intuitive plots were created, establishing trends for each geometry type and their respective effective properties. Any TPMS structures would benefit applications that prioritize only high heat transfer rates. However, if high fluid flow is equally valued, the lattice and HF-type structures might be more suitable. And if high heat transfer, fluid flow, and stiffness are all equally important for an application, the HF structure is the most obvious option, followed by the TPMS. If low fluid flow and low heat transfer are desired, the stochastic structure will continue to be valuable.

- The HF permeability was strongly correlated to the perforation factor, which controls the size of the perforating hole. With this parameter, the dimensionless permeability could be adjusted by an order of magnitude for the HF structures.
- When compared with effective thermal conductivity results for commercial stochastic foams, the lattice, HF, and TPMS structures exhibited, on average, 172%, 179%, and 243% the effective thermal conductivities at the same porosity, respectively.
- When the dimensionless permeability is plotted versus the dimensionless thermal conductivity, the structures fall into four distinct categories: low thermal conductivity and low permeability for the stochastic structures, large range of permeability and good thermal conductivity for the HF structures, extremely high permeability and good thermal conductivity for the lattice structures, and mid-level permeability and great thermal conductivity for the TPMS structures tested.
- The TPMS and HF structures showed stretching dominant behavior, while the lattice structures showed bending dominant behavior.
- The HF structure showed significantly higher tunability in both permeability and mechanical stiffness than other structures simulated.

Data availability

Data will be made available on request.

Declaration of Competing Interest

The authors declare that they have no known competing financial interests or personal relationships that could have appeared to influence the work reported in this paper.

Acknowledgment

S.S. and X.L. highly appreciate the funding support by Kansas NASA EPSCoR Research Infrastructure Development Program (Award: 80NSSC19M0042). X.L. wants to acknowledge NASA EPSCoR (Award: 80NSSC22M0221) and the startup fund from Washington University in St. Louis for supporting this study. Y. C. gratefully acknowledges the financial support of the National Science Foundation, CMMI Mechanics of Materials and Structures Program (Award Number: 2114823).

References

[1] H. Safari, B.J. Balcom, A. Afrough, Characterization of pore and grain size distributions in porous geological samples – An image processing workflow, Comput. Geosci. 156 (2021), https://doi.org/10.1016/J.CAGEO.2021.104895 104895.
[2] M. Camargo, P.R. Cleto, M.A. Maedo, E.A. Rodrigues, L.A.G. Bitencourt, O.L. Manzoli, Modeling the hydrodynamic behavior of fractures and barriers in porous media using coupling finite elements, J. Pet. Sci. Eng. 208 (2022), https://doi.org/10.1016/j.petrol.2021.109700.
[3] Q. Lyu, H. Wu, X. Li, A 3D model reflecting the dynamic generating process of pore networks for geological porous media, Comput. Geotech. 140 (2021), https://doi.org/10.1016/j.compgeo.2021.104444 104444.
[4] S. Sen, C.V. Srinivas, R. Venkatesan, A probabilistic model for the simulation of radioactivity transport through a heterogeneous porous medium, Prog. Nucl. Energy 145 (2022), https://doi.org/10.1016/j.pnucene.2021.104101 104101.
[5] W.F. Ho, H.K. Tsou, S.C. Wu, W.Y. Hsiao, H.C. Hsu, Characteristics and structure of porous TNM alloy for biomedical applications, Resul. Mater. 11 (2021), https://doi.org/10.1016/j.rinma.2021.100212 100212.
[6] J.-Y. Zeng, X.-S. Wang, Y.-X. Sun, X.-Z. Zhang, Research progress in AIE-based crystalline porous materials for biomedical applications, Biomaterials 286 (2022), https://doi.org/10.1016/j.biomaterials.2022.121583 121583.
[7] W. Tian, Y. Wang, J. Xu, H. Li, G. Song, M. Ding, Z. Kang, Y. Yin, A. Wang, P. Ning, F. Dong, J. Wang, Evaluation of the biomedical properties of a Ca+-conjugated silk fibroin porous material, Mater. Sci. Eng. C 104 (2019), https://doi.org/10.1016/j.msec.2019.110003 110003.
[8] L. Guo, S. Ataollah Naghavi, Z. Wang, S. Nath Varma, Z. Han, Z. Yao, L. Wang, L. Wang, C. Liu, On the design evolution of hip implants: A review, Mater. Des. 216 (2022), https://doi.org/10.1016/j.matdes.2022.110552 110552.
[9] Y. Lv, G. Liu, B. Wang, Y. Tang, Z. Lin, J. Liu, G. Wei, L. Wang, Pore Strategy Design of a Novel NiTi-Nb Biomedical Porous Scaffold Based on a Triply Periodic Minimal Surface, Front. Bioeng. Biotechnol. 10 (2022), https://doi.org/10.3389/fbioe.2022.910475 910475.
[10] D. Lehmhus, M. Vesenjak, S. Schampheleire, T. Fiedler, From Stochastic Foam to Designed Structure: Balancing Cost and Performance of Cellular Metals, Materials. 10 (2017) 922, https://doi.org/10.3390/ma10080922.
[11] C.Y. Zhao, T. Kim, T.J. Lu, H.P. Hodson, Thermal Transport in High Porosity Cellular Metal Foams, J. Thermophys Heat Transfer 18 (3) (2004) 309–317.
[12] M. Sun, M. Fan, L. Li, Z. Xu, T. Yang, Thermal conductivity of aluminum foam based on 3-D stochastic sphere model, Heat Transfer. 49 (2020) 823–837, https://doi.org/10.1002/htj.21640.
[13] A. du Plessis, S.M.J. Razavi, M. Benedetti, S. Murchio, M. Leary, M. Watson, D. Bhate, F. Berto, Properties and applications of additively manufactured metallic cellular materials: a review, Prog. Mater Sci. 125 (2022), https://doi.org/10.1016/j.pmatsci.2021.100918.
[14] A. Schoen, Infinite periodic minimal surfaces without self-intersections, NASA Technical Note (TN). (1970) 19700020472.
[15] E. Lord, A. Mackay, Periodic minimal surfaces of cubic symmetry, Curr. Sci. 85 (2003) 346–362.
[16] J. Feng, J. Fu, X. Yao, Y. He, Triply periodic minimal surface (TPMS) porous structures: from multi-scale design, precise additive manufacturing to multidisciplinary applications, Int. J. Extrem. Manufactur. 4 (2) (2022), https://doi.org/10.1088/2631-7990/ac5be6.
[17] F. Wang, H. Jiang, Y. Chen, X. Li, Predicting thermal and mechanical performance of stochastic and architected foams, Int. J. Heat Mass Transf. 171 (2021), https://doi.org/10.1016/j.ijheatmasstransfer.2021.121139 121139.
[18] Z.A. Qureshi, S.A.B. Al-Omari, E. Elnajjar, O. Al-Ketan, R.A. Al-Rub, Using triply periodic minimal surfaces (TPMS)-based metal foams structures as skeleton for metal-foam-PCM composites for thermal energy storage and energy management applications, Int. Commun. Heat Mass Transfer 124 (2021), https://doi.org/10.1016/j.icheatmasstransfer.2021.105265 105265.

[19] Z. Ahmed Qureshi, E. Elnajjar, O. Al-Ketan, R. Abu Al-Rub, S. Burhan Al-Omari, Heat transfer performance of a finned metal foam-phase change material (FMF-PCM) system incorporating triply periodic minimal surfaces (TPMS), Int. J. Heat Mass Transf. 170 (2021), https://doi.org/10.1016/j.ijheatmasstransfer.2021.121001 121001.
[20] G.L. Vignoles, D. Rochais, S. Chupin, Computation of the conducto-radiative effective heat conductivity of porous media defined by Triply Periodic Minimal Surfaces, Int. J. Therm. Sci. 159 (2021), https://doi.org/10.1016/j.ijthermalsci.2020.106598 106598.
[21] D.W. Abueidda, R.K. Abu Al-Rub, A.S. Dalaq, D.W. Lee, K.A. Khan, I. Jasiuk, Effective conductivities and elastic moduli of novel foams with triply periodic minimal surfaces, Mech. Mater. 95 (2016) 102–115, https://doi.org/10.1016/j.mechmat.2016.01.004.
[22] G.L. Vignoles, A hybrid random walk method for the simulation of coupled conduction and linearized radiation transfer at local scale in porous media with opaque solid phases, Int. J. Heat Mass Transf. 93 (2016) 707–719, https://doi.org/10.1016/j.ijheatmasstransfer.2015.10.056.
[23] H. Jiang, H. Ziegler, Z. Zhang, H. Meng, D. Chronopoulos, Y. Chen, Mechanical properties of 3D printed architected polymer foams under large deformation, Mater. Des. 194 (2020), https://doi.org/10.1016/j.matdes.2020.108946 108946.
[24] Rhinoceros 3D [Geometry modeling software]. Robert McNeel & Associates; 2021. Available from: https://www.rhino3d.com/.
[25] nTopology [Geometry modeling software]. nTopology, Inc.; 2022. Available from: https://ntopology.com.
[26] F. Wang, X. Li, The stagnant thermal conductivity of porous media predicted by the random walk theory, Int. J. Heat Mass Transf. 107 (2017) 520–533, https://doi.org/10.1016/j.ijheatmasstransfer.2016.11.069.
[27] F. Wang, G.A. Riley, M. Egbo, M.M. Derby, G. Hwang, X. Li, Integrated micro x-ray tomography and pore-scale simulations for accurate permeability predictions of porous media, Front. Heat Mass Transfer. 15 (2020) 1, https://doi.org/10.5098/hmt.15.1.
[28] L. Gong, Y. Wang, X. Cheng, R. Zhang, H. Zhang, A novel effective medium theory for modelling the thermal conductivity of porous materials, Int. J. Heat Mass Transf. 68 (2014) 295–298, https://doi.org/10.1016/j.ijheatmasstransfer.2013.09.043.
[29] K. Pietrak, T.S. Wisniewski, A review of models for effective thermal conductivity of composite materials, J. Power Technol. 95 (2015) 14–24.
[30] T.L. Bergman, A.S. Lavine, F.P. Incropera, D.P. DeWitt, Fundamentals of Heat and Mass Transfer, 8th ed., Wiley, 2018.
[31] M. Danielsson, D.M. Parks, M.C. Boyce, Three-dimensional micromechanical modeling of voided polymeric materials, J. Mech. Phys. Solids 50 (2002) 351–379, https://doi.org/10.1016/S0022-5096(01)00060-6.
[32] M. Danielsson, D.M. Parks, M.C. Boyce, Micromechanics, macromechanics and constitutive modeling of the elasto-viscoplastic deformation of rubber-toughened glassy polymers, J. Mech. Phys. Solids 55 (2007) 533–561, https://doi.org/10.1016/j.jmps.2006.08.006.
[33] L. Wang, M.C. Boyce, C.-Y. Wen, E.L. Thomas, Plastic Dissipation Mechanisms in Periodic Microframe-Structured Polymers, Adv. Funct. Mater. 19 (2009) 1343–1350, https://doi.org/10.1002/adfm.200801483.
[34] R. Hedayati, M. Sadighi, M. Mohammadi Aghdam, A. Zadpoor, Mechanical Properties of Additively Manufactured Thick Honeycombs, Materials. 9 (2016) 613, https://doi.org/10.3390/ma9080613.
[35] M.A. Schuetz, L.R. Glicksman, A Basic Study of Heat Transfer Through Foam Insulation, J. Cell. Plast. 20 (1984) 114–121, https://doi.org/10.1177/0021955X8402000203.
[36] H.S. Abdulhadi, A. Fadeel, T.A. Alwattar, A. Mian, Developing scaling laws to predict compressive mechanical properties and determine geometrical parameters of modified BCC lattice structures, Eng. Rep. 5 (2) (2023).